

RESEARCH

Open Access



Gaussian processes based extended target tracking in polar coordinates with input uncertainty

Yunfei Guo^{*†} , Dongsheng Yang[†], Lei Ren[†] and Lei Yan[†]

[†]Yunfei Guo, Dongsheng Yang, Lei Ren and Lei Yan contributed equally to this work

*Correspondence:
gyf@hdu.edu.cn

School of Automation, Hangzhou Dianzi University, Second Street, Hangzhou 310018, Zhejiang, China

Abstract

Gaussian processes (GP) based extended target tracking (ETT) technique has attracted the attention of scientists since it can accurately estimate the kinematic states as well as the contour states of irregular-shape targets. Most traditional GP methods consider the ETT problem with a linear measurement model in Cartesian coordinates and ignore the input uncertainty of GP for simplicity. In many applications, however, measurements are generated with high-resolution sensors in polar coordinates. More importantly, the ignorance of input uncertainty in GP will exacerbate the tracking performance in these cases. In order to track an irregular-shape extended target in polar coordinates with input uncertainty, an improved GP-based probabilistic data association (IGP-PDA) algorithm is developed that includes the following enhancements: Firstly, a nonlinear measurement model is used and the unbiased converted measurement technique is invoked for the ETT problem. Secondly, the analytical form of statistical properties of the input uncertainty due to measurements noise and predicted error is derived. Thirdly, an IGP-PDA taking into account measurement origin uncertainty as well as input uncertainty is proposed, and three sub-optimal implementations are provided. Last, the posterior Cramer-Rao lower bound of ETT with input uncertainty is derived. Simulation results verify the effectiveness of the proposed method.

Keywords: Extended target tracking, Gaussian processes, Input uncertainty, Nonlinear measurement, Measurement origin uncertainty

1 Introduction

With the rapid development in high-resolution sensor technology, extended target tracking (ETT) is attracting more and more attention with applications in military and civilian fields, such as automotive active safety systems [1, 2], advanced driver assistance systems [3, 4], maritime and ground surveillance [5, 6], robotic and control [7] and points cloud processing [8–10]. For the problem of ETT, a target is assumed to have multiple random scattering points and hence may yield multiple measurements per scan. The objective of ETT is to estimate the kinematic state along with the contour state of the target of interest [11].

Many ETT methods have been proposed in the last decades, such as Sequential Monte Carlo (SMC) [12, 13], Random Matrix (RM) [14–18], Random Hypersurface Models (RHM) [19–21], Gaussian Processes based ETT (GP-ETT) [6, 22, 23], and so on. Among these works, the GP has the ability to model and learn an unknown radius function of an irregular-shape target analytically and can provide benefits toward higher-precision contour estimation [24]. In [22], a GP-based extended Kalman filter (GP-EKF) is proposed for ETT in a benign scenario in the absence of clutter. Moreover, the GP model is combined with the labeled multi-Bernoulli filter for tracking multiple extended targets [25]. In order to track a non-rigid and asymmetric extended target, a Spatio-temporal GP-based ETT technique is proposed in [23]. The above GP-ETT algorithms verify the contour estimation ability of GP in the benign scenario, ignoring the effect of the measurement origin uncertainty on the tracker. In some applications, e.g., tracking the ships in the ocean, the high-resolution sensor receives a lot of measurements not only from targets but also from sea clutter. In this case, the measurement origin uncertainty must be taken into account. To address the problem of ETT in clutter, the GP-based probabilistic data association (GP-PDA) is proposed in [26] and the posterior Cramer-Rao lower bound (PCRLB) is derived to evaluate the performance of ETT with measurement origin uncertainty. Besides, the GP-PDA is combined with the interacting multiple model (IMM) to simultaneously track a ship and its wake in [6]. As mentioned above, to track extended targets in clutter, the GP-PDA approach seems very promising since the fact that it can not only estimate the kinematic state but also give a precise contour state of the irregular-shape target.

Most previous GP methods mentioned above assume that the ETT measurement model is linear and the GP input is known accurately for simplicity. This assumption is reasonable in civilian applications but does not hold in many military applications. In maritime surveillance, for example, high-resolution maritime radars are used to measure the range, bearing, and Doppler of the target in polar coordinates and cannot provide position measurements directly. In other words, a nonlinear measurement model is more suitable in this case. Moreover, the input uncertainty of GP, caused by poor bearing resolution and imprecise state prediction, will significantly affect the tracking performance of ETT and cannot be ignorable. In the GP literature, there are two categories to deal with the uncertain input [27]. The first category, called heteroscedastic GP models, transforms the input variance into a parameter that varies with the output residual by changing the distribution of the output noise [28–30]. However, this approximate method ignores the structure of the uncertain inputs. Another category deals with the uncertain input directly in the prediction phase and generally approximates the mean and variance of the prediction distribution of GP [31–34]. Further research is developed in [35, 36] where a noise-input GP model was considered both in the prediction phase and in the training phase.

In this paper, we consider the problem of tracking the irregular-shape extended targets in polar coordinates with input uncertainty along with measurement origin uncertainty. This work is an extension of the author's previous results presented in [26]. Under the GP-PDA framework, the measurement origin uncertainty can be effectively solved. In order to modify the effect of input uncertainty on the tracking

performance of GP-ETT, an improved GP-based probabilistic data association (IGP-PDA) algorithm is proposed to track an extended target in clutter. The main contributions of this paper are as follows:

- The analytical statistical property of the uncertain input is derived:

The unbiased converted measurement (UCM) technique [37] is invoked to transform raw nonlinear measurements into unbiased linear measurements. The uncertain input of GP is assumed to be Gaussian distribution [27] and its statistical property is given analytically using the measurement noise variance, converted bias covariance, and the state predicted covariance.

- Three approximation implementations are given to solve the uncertain input:

An IGP-PDA algorithm taking into account uncertain input is proposed, where the prediction distribution of GP is modified with the statistical property of uncertain input. Since the analytical solution to the prediction distribution of GP is not available in most cases, three approximation implementations are given.

- A new posterior Cramer-Rao lower bound is derived:

In order to evaluate the tracking performance of ETT, a new posterior Cramer-Rao lower bound (PCRLB) of ETT considering not only the measurement origin uncertainty but also the input uncertainty is derived. As a larger covariance of GP prediction distribution due to input uncertainty is included, the new performance bound is more conservative and reasonable than the previous result in [26].

The remainder of this paper is structured as follows. Section 2 introduces the background of standard GP and GP with uncertain input. Section 3 describes the ETT problem in polar coordinates with measurement origin uncertainty. In Sect. 4, the statistical property of the uncertain input and the IGP-PDA algorithm is proposed. Section 5 derives a more reasonable PCRLB of ETT. Simulation and conclusions are presented in Sects. 6 and 6, respectively.

2 Background

The standard GP and the GP with uncertain input are reviewed briefly in this section, that forms the foundation of the proposed method.

2.1 Standard Gaussian processes

A Gaussian process is a generalization of the multivariate Gaussian distribution suitable for learning the distribution of an unknown function, and it can make inferences in the function-space view. Consider a function as follows:

$$y = f(u) + \epsilon, \quad (1)$$

where u is the input of latent function $f(\cdot)$, y is the noisy output, and $\epsilon \sim \mathcal{N}(0, \sigma_\epsilon^2)$ is a Gaussian distributed noise. Under the GP framework, the latent function $f(\cdot)$ can be described by the mean function $a(u)$ and covariance function $\kappa(u, u')$ as follows:

$$f(u) \sim \mathcal{GP}(a(u), \kappa(u, u')). \quad (2)$$

Given a training set \mathcal{D} of N_{gp} observations, $\mathcal{D} = \{(u_i, y_i) \mid i = 1, \dots, N_{gp}\}$, where u_i denotes the i^{th} training input and y_i the corresponding training output. Denote $\mathbf{u} = [u_1, \dots, u_{N_{gp}}]$ and $\mathbf{y} = [y_1, \dots, y_{N_{gp}}]$ as the training input vector and training output vector, respectively. The objective of GP is to use a set of training data $\mathcal{D} = [\mathbf{u}, \mathbf{y}]$ to learn the unknown latent function $f(\cdot)$, or the predictive distribution of the function outputs given the inputs [24].

For a test input u_* , since the joint distribution is a Gaussian, the predictive distribution $p(f(u_*) \mid u_*, \mathcal{D})$ is also Gaussian with mean $\mu_{SGP}(u_*)$ and variance $v_{SGP}(u_*)$ [33]

$$p(f(u_*) \mid u_*, \mathcal{D}) \sim \mathcal{N}(\mu_{SGP}(u_*), v_{SGP}(u_*)) \quad (3)$$

where

$$\mu_{SGP}(u_*) = a(u_*) + K(u_*, \mathbf{u}) [K(\mathbf{u}, \mathbf{u}) + \sigma_\epsilon^2 I]^{-1} (\mathbf{y} - a(\mathbf{u})) \quad (4)$$

$$v_{SGP}(u_*) = K(u_*, u_*) - K(u_*, \mathbf{u}) [K(\mathbf{u}, \mathbf{u}) + \sigma_\epsilon^2 I]^{-1} K(\mathbf{u}, u_*) \quad (5)$$

where I is an $N_{gp} \times N_{gp}$ identity matrix, $K(\cdot, \cdot)$ is a matrix of covariance function, and

$$K(\mathbf{u}, \mathbf{u}) = \begin{bmatrix} \kappa(u_1, u_1) & \dots & \kappa(u_1, u_{N_{gp}}) \\ \vdots & \ddots & \vdots \\ \kappa(u_{N_{gp}}, u_1) & \dots & \kappa(u_{N_{gp}}, u_{N_{gp}}) \end{bmatrix} \quad (6)$$

$$K(\mathbf{u}, u_*) = K(u_*, \mathbf{u})^\top = [\kappa(u_1, u_*), \dots, \kappa(u_{N_{gp}}, u_*)] \quad (7)$$

Herein, the prediction mean $\mu_{SGP}(u_*)$ serves as an estimate of the latent function $f(u_*)$ with the uncertainty of $\sqrt{v_{SGP}(u_*)}$.

2.2 Gaussian processes with uncertain input

Usually, the input of GP u_* is assumed to be accurately known and noise-free. However, this assumption does not hold in some applications. For example, in a discrete-time series analysis problem, the current input is estimated from the last step. For a GP model that ignores the cumulative prediction variance, its model is not conservative enough, which makes the prediction accompanied by unrealistic small uncertainty [31]. Assume that the uncertain input of latent function u_* follows a Gaussian distribution with mean μ_{u_*} and variance Σ_{u_*} [32], the prediction distribution can be obtained by

$$p(f(u_*) \mid \mu_{u_*}, \Sigma_{u_*}, \mathcal{D}) = \int p(f(u_*) \mid u_*, \mathcal{D}) p(u_*) du_* \quad (8)$$

where $p(f(u_*) \mid u_*, \mathcal{D})$ is a Gaussian distribution with mean $\mu_{SGP}(u_*)$ and variance $v_{SGP}(u_*)$ given by (4) and (5), respectively. Some methods are proposed to approximate the above integral of prediction distribution since it is analytically intractable. For example, the numerical approximation method and the Taylor Series approximation method.

In numerical approximation, the general solution of (8) can be defined as [27]:

$$\begin{aligned}
 p(f(u_*) | \mu_{u_*}, \Sigma_{u_*}, \mathcal{D}) &= \int p(f(u_*) | u_*, \mathcal{D}) p(u_*) du_* \\
 &\approx \frac{1}{N_t} \sum_{i=1}^{N_t} p(f(u_*) | u_i^*, \mathcal{D})
 \end{aligned} \quad (9)$$

where u_i^* is the i th random or determinate sample from $p(u^*)$, N_t denotes the number of sampling.

In Taylor Series approximation, the analytic Gaussian approximation only needs the first two moments of $p(f(u_*) | \mu_{u_*}, \Sigma_{u_*}, \mathcal{D})$. They are obtained by the law of iterated expectation and the law of conditional variances [31]:

$$\mu_{\text{IGP}}(u_*) = \mathbb{E}_{u_*} [\mathbb{E}_{f(u_*)} [f(u_*) | u_*]] = \mathbb{E}_{u_*} [\mu_{\text{SGP}}(u_*)] \approx \mu_{\text{SGP}}(\mu_{u_*}) \quad (10)$$

where

$$\mu_{\text{SGP}}(\mu_{u_*}) = K(\mu_{u_*}, \mathbf{u}) [K(\mathbf{u}, \mathbf{u}) + \sigma_\epsilon^2 I]^{-1} \mathbf{y} \quad (11)$$

The predictive variance is given as

$$\begin{aligned}
 v_{\text{IGP}}(u_*) &= \mathbb{E}_{u_*} [v_{\text{SGP}}(u_*)] + \text{var}_{u_*} [\mu_{\text{SGP}}(u_*)] \\
 &\approx v_{\text{SGP}}(\mu_{u_*}) + \frac{\partial \mu_{\text{SGP}}(u_*)}{\partial \mathbf{u}_*} \Big|_{\mathbf{u}_* = \mu_{u_*}}^\top \Sigma_{u_*} \frac{\partial \mu_{\text{SGP}}(u_*)}{\partial \mathbf{u}_*} \Big|_{\mathbf{u}_* = \mu_{u_*}}
 \end{aligned} \quad (12)$$

where

$$v_{\text{SGP}}(\mu_{u_*}) = K(\mu_{u_*}, \mu_{u_*}) - K(\mu_{u_*}, \mathbf{u}) [K(\mathbf{u}, \mathbf{u}) + \sigma_\epsilon^2 I]^{-1} K(\mathbf{u}, \mu_{u_*}) \quad (13)$$

The input uncertainty does not provide any correction for the prediction expectation of GP. However, it provides a correction term of zero-order to the variance of prediction, and more details refer to [31].

3 Dynamic and measurement models

In this section, the GP-based dynamic model and the measurement model of ETT are provided in 2D space, more details see [22, 26]. Herein the measurement model is established in polar coordinates with measurement origin uncertainty.

Consider the following dynamic model of an irregular-shape extended target

$$\mathcal{X}_k = F_{k-1} \mathcal{X}_{k-1} + \mathbf{v}_{k-1} \quad (14)$$

where $\mathcal{X}_k = [(\mathbf{x}_k^s)^\top, (\mathbf{x}_k^f)^\top]^\top$ is the extended target state at time k , \mathbf{x}_k^s and \mathbf{x}_k^f denote the kinematic state and contour state, respectively. The term $F_{k-1} = \text{diag}\{F_{k-1}^s, F_{k-1}^f\}$ is state transition matrix and $\mathbf{v}_{k-1} = [(\mathbf{v}_{k-1}^s)^\top, (\mathbf{v}_{k-1}^f)^\top]^\top$ is a zero-mean white Gaussian noise with covariance matrix $Q_{k-1} = \text{diag}\{Q_{k-1}^s, Q_{k-1}^f\}$. The specific form of state transition matrix and covariance matrix will be given in the simulation. Then, the Eq. (14) can be rewritten as

$$\begin{bmatrix} \mathbf{x}_k^s \\ \mathbf{x}_k^f \end{bmatrix} = \begin{bmatrix} F_{k-1}^s & 0 \\ 0 & F_{k-1}^f \end{bmatrix} \begin{bmatrix} \mathbf{x}_{k-1}^s \\ \mathbf{x}_{k-1}^f \end{bmatrix} + \begin{bmatrix} \mathbf{v}_{k-1}^s \\ \mathbf{v}_{k-1}^f \end{bmatrix} \quad (15)$$

where the kinematic state $\mathbf{x}_k^s = [x_k, \dot{x}_k, y_k, \dot{y}_k, \phi_k, \dot{\phi}_k]^\top$ is a six-dimension vector, which is composed of the target centroid position $\mathbf{x}_k^c \triangleq [x_k, y_k]^\top$, the target velocity $[\dot{x}_k, \dot{y}_k]^\top$, the heading ϕ_k and the heading rate $\dot{\phi}_k$. The contour state is denoted as $\mathbf{x}_k^f = [f(\theta_{k,1}), f(\theta_{k,2}), \dots, f(\theta_{k,N})]^\top$, where $\theta_{k,i}$ and $f(\theta_{k,i})$, $1 \leq i \leq N$, are the angle and the unknown radius function of the i th contour point, respectively, and N is the number of contour points. Usually, the prior knowledge of the target contour is unavailable, and the angle of contour point $\theta_{k,i} \in [0, 2\pi)$ can be chosen as $\theta_{k,i} = 2\pi(i-1)/N$, $1 \leq i \leq N$. In addition, all angles of the contour points are stacked into a vector as $\Theta \triangleq [\theta_{k,1}, \dots, \theta_{k,N}]^\top$. The unknown radius function $f(\theta_{k,i})$ can be described by a GP model as follows

$$f(\theta_k) \sim \mathcal{GP}(a(\theta_k), \kappa(\theta_k, \theta'_k)) \quad (16)$$

Without loss of generality, the mean function is assumed to follow $a(\theta_k) \sim \mathcal{N}(0, \sigma_r^2)$, and the covariance function can be chosen as a modified squared exponential function

$$\kappa(\theta_k, \theta'_k) = \sigma_f^2 e^{-\frac{2 \sin^2(|\theta_k - \theta'_k|/2)}{l^2}} \quad (17)$$

to encode the periodicity of angle θ_k [22], where σ_f and l are the hyper-parameters of GP.

An extended target has multiple fluctuating scattering points, which may appear on or within the contour. These scattering points may generate multiple noisy measurements per scan. Previous work usually assumes that the sensor can obtain the positions of scattering points directly and invoke a measurement model in Cartesian coordinates. However, many types of sensors, such as radar and sonar, can only measure the range and bearing of the scattering points in polar coordinates. In this subsection, a generalized nonlinear measurement model with measurement origin uncertainty is presented.

Suppose that there are M_k measurements at time k . In view of the measurement origin uncertainty, the j th measurement, denoted as $c_{k,j} = [d_{k,j}, \beta_{k,j}]^\top$, $1 \leq j \leq M_k$, may be originated from a scattering point of the target or from clutter, where $d_{k,j}$ and $\beta_{k,j}$ denote the range and bearing, respectively. Thus, a generalized nonlinear measurement model is given as follows.

$$c_{k,j} = \begin{cases} \left[\begin{array}{c} \sqrt{(z_{k,j}^\xi)^2 + (z_{k,j}^\eta)^2} \\ \arctan(\frac{z_{k,j}^\eta}{z_{k,j}^\xi}) \end{array} \right] + w_{k,j}^{\text{pol}} & \text{from target} \\ \underbrace{\left[\begin{array}{c} \mathbf{h}_{k,j}^{\text{pol}}(z_{k,j}) + w_{k,j}^{\text{pol}} \\ \chi_{k,j} \end{array} \right]}_{\text{from clutter}} & \text{from clutter} \end{cases} \quad (18)$$

For a clutter-originated measurement, the clutter $\chi_{k,j}$ is assumed to follow a uniform spatial distribution and a Poisson cardinality distribution with parameter λ_c . For a target-originated measurement, the nonlinear function $\mathbf{h}_{k,j}^{\text{pol}}(z_{k,j})$ represents the noise-free measurement and $w_{k,j}^{\text{pol}} \sim \mathcal{N}(0, R^{\text{pol}})$ is the measurement noise in polar coordinates, $R^{\text{pol}} = \text{diag}\{\sigma_d^2, \sigma_\beta^2\}$.

In the above equation, $z_{k,j} = [z_{k,j}^\xi, z_{k,j}^\eta]^\top$ denotes the x -axis and y -axis position of the scattering point corresponding to the j th measurement (see Fig. 1). For simplicity, the

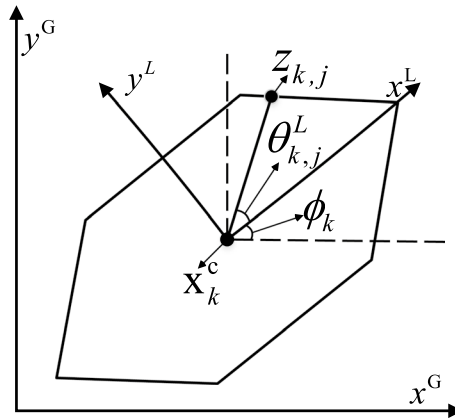


Fig. 1 Geometric relationship between $\theta_{k,j}^L$, $z_{k,j}$, and ϕ_k

scattering points are assumed to distribute along the contour of the target here. In this case, the position of scattering point $z_{k,j}$ is given by

$$z_{k,j} = \mathbf{h}_{k,j}^{\text{car}}(\mathcal{X}_k) = \mathbf{x}_k^c + \mathbf{p}_{k,j} f(\theta_{k,j}^L) \quad (19)$$

where $\mathbf{h}_{k,j}^{\text{car}}(\mathcal{X}_k)$ denotes the measurement function in the Cartesian coordinates, $\mathbf{p}_{k,j}$ is the orientation vector and $\theta_{k,j}^L$ is the angle of the scattering point $z_{k,j}$ relative to the target centroid \mathbf{x}_k^c in local coordinates, more details see [22]. In addition, $f(\theta_{k,j}^L)$ is a unknown radius function and can be rewritten as follows with the GP model.

$$f(\theta_{k,j}^L) = \mu_{\text{SGP}}(\theta_{k,j}^L) + w_{k,j}^f \quad (20)$$

$$\mu_{\text{SGP}}(\theta_{k,j}^L) = K(\theta_{k,j}^L, \Theta)[K(\Theta, \Theta)]^{-1} \mathbf{x}^f \quad (21)$$

where $\mu_{\text{SGP}}(\theta_{k,j}^L)$ is the prediction mean of $p(f(\theta_{k,j}^L) | \theta_{k,j}^L, \Theta)$, and $w_{k,j}^f \sim \mathcal{N}(0, v_{\text{SGP}}(\theta_{k,j}^L))$ is a zero-mean white Gaussian noise of radius function with the following variance

$$v_{\text{SGP}}(\theta_{k,j}^L) = \kappa(\theta_{k,j}^L, \theta_{k,j}^L) - K(\theta_{k,j}^L, \Theta)[K(\Theta, \Theta)]^{-1} K(\Theta, \theta_{k,j}^L) \quad (22)$$

Then, substitute the above equations into (18), the target-originated measurement in polar coordinate can be rewritten as

$$\begin{aligned} c_{k,j} &= \mathbf{h}_{k,j}^{\text{pol}}(z_{k,j}) + w_{k,j}^{\text{pol}} \\ &= \mathbf{h}_{k,j}^{\text{pol}}(\mathbf{x}_k^c + \mathbf{p}_{k,j} f(\theta_{k,j}^L)) + w_{k,j}^{\text{pol}} \\ &= \mathbf{h}_{k,j}^{\text{pol}}(\mathbf{x}_k^c + \mathbf{p}_{k,j} (\mu_{\text{GP}}(\theta_{k,j}^L) + w_{k,j}^f)) + w_{k,j}^{\text{pol}} \end{aligned} \quad (23)$$

Denote the measurement set as $\mathcal{C}_k = \{c_{k,j}\}_{j=1}^{M_k}$ at time k . The main objective of ETT is to estimate the kinematic state \mathbf{x}_k^s and the contour state \mathbf{x}_k^f of the extended target from a total measurement set $\mathcal{C}_{1:k} \triangleq \{\mathcal{C}_1, \dots, \mathcal{C}_k\}$ up to and including time k .

4 Methodology

In this section, the statistical properties of the uncertain input of GP-ETT are derived. Then an improved GP-PDA algorithm is proposed accounting for input uncertainty. Also, three approximation implementations are provided since the analytical solution of prediction distribution is unavailable in most cases.

4.1 Statistical properties of uncertain input

Under the framework of GP-ETT [22], the GP input is the angle of scattering point relative to the target centroid in local coordinates and it is given as

$$\theta_{k,j}^L = \arctan \left(\frac{z_{k,j}^\eta - y_k}{z_{k,j}^\xi - x_k} \right) - \phi_k \quad (24)$$

where $z_{k,j} = [z_{k,j}^\xi, z_{k,j}^\eta]^\top$ denotes the position vector of the scattering point corresponding to the j th measurement, $\mathbf{x}_k^c = [x_k, y_k]^\top$ denotes the position vector of target centroid, and ϕ_k denotes the heading of target. Note that the above variables $z_{k,j}$, \mathbf{x}_k^c and ϕ_k are all unknown to the tracker.

They are replaced by their observations and estimates in actual processing [22, 26] and hence yield the input uncertainty (see Fig. 2). Therein, the term $\theta_{k,j}^G = \theta_{k,j}^L + \phi_k$ is the angle of scattering point relative to the target centroid in global coordinates. The true distribution of GP input $\theta_{k,j}^L$ is intractable even if all the above variables are Gaussian distributed. For simplicity, the GP input is assumed to follow a Gaussian distribution [23, 31], i.e., $\theta_{k,j}^L \sim \mathcal{N}(\mu_{\theta_{k,j}^L}, \Sigma_{\theta_{k,j}^L})$. The mean of GP input $\mu_{\theta_{k,j}^L}$ is approximated as

$$\mu_{\theta_{k,j}^L} = \mathbb{E} \left[\arctan \left(\frac{z_{k,j}^\eta - y_k}{z_{k,j}^\xi - x_k} \right) - \phi_k \right] \quad (25)$$

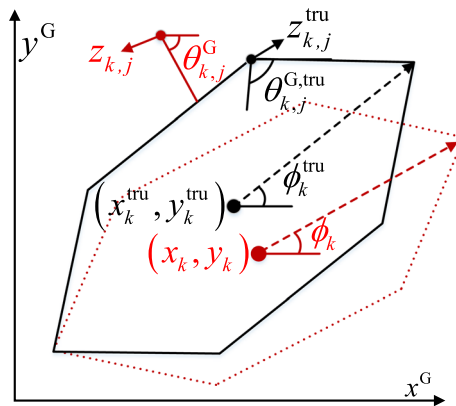


Fig. 2 Actual meaning of the input uncertainty in GP-ETT: red dashed line and variables represent the contour estimates state and the corresponding variables; black solid line and variables denote the truth contour state and the corresponding variables

$$\approx \arctan \left(\frac{c_{k,j}^{\mathbf{u},\eta} - \hat{y}_{k|k-1}}{c_{k,j}^{\mathbf{u},\xi} - \hat{x}_{k|k-1}} \right) - \hat{\phi}_{k|k-1} \quad (26)$$

where $\mathbf{c}_{k,j}^{\mathbf{u}} \triangleq [c_{k,j}^{\mathbf{u},\xi}, c_{k,j}^{\mathbf{u},\eta}]^T$ is the linear measurement converted from $c_{k,j}$ via UCM technique [37], more details see “Appendix 1”. $[\hat{x}_{k|k-1}, \hat{y}_{k|k-1}]^T$ and $\hat{\phi}_{k|k-1}$ are the position prediction of target centroid and the heading prediction, respectively. They can be predicted from the dynamic model with the state estimate at time $k-1$.

Now the variance of input $\Sigma_{\theta_{k,j}^L}$ can be derived as follows according to the error propagation theory [27].

$$\begin{aligned} \Sigma_{\theta_{k,j}^L} &= \tilde{\sigma}_{c1}^2 \left(\frac{\partial \theta_{k,j}^L}{\partial c_{k,j}^{\mathbf{u},\xi}} \right)^2 + \tilde{\sigma}_{c2}^2 \left(\frac{\partial \theta_{k,j}^L}{\partial c_{k,j}^{\mathbf{u},\eta}} \right)^2 \\ &\quad + \tilde{\sigma}_{xx}^2 \left(\frac{\partial \theta_{k,j}^L}{\partial \hat{x}_{k|k-1}} \right)^2 + \tilde{\sigma}_{yy}^2 \left(\frac{\partial \theta_{k,j}^L}{\partial \hat{y}_{k|k-1}} \right)^2 + \tilde{\sigma}_{\phi\phi}^2 \left(\frac{\partial \theta_{k,j}^L}{\partial \hat{\phi}_{k|k-1}} \right)^2 \\ &= \tilde{\sigma}_{c1}^2 \left[\frac{c_{k,j}^{\mathbf{u},\xi} - \hat{x}_{k|k-1}}{(c_{k,j}^{\mathbf{u},\xi} - \hat{x}_{k|k-1})^2 + (c_{k,j}^{\mathbf{u},\eta} - \hat{y}_{k|k-1})^2} \right]^2 \\ &\quad + \tilde{\sigma}_{c2}^2 \left[\frac{c_{k,j}^{\mathbf{u},\eta} - \hat{y}_{k|k-1}}{(c_{k,j}^{\mathbf{u},\xi} - \hat{x}_{k|k-1})^2 + (c_{k,j}^{\mathbf{u},\eta} - \hat{y}_{k|k-1})^2} \right]^2 \\ &\quad + \tilde{\sigma}_{xx}^2 \left[\frac{c_{k,j}^{\mathbf{u},\eta} - \hat{y}_{k|k-1}}{(c_{k,j}^{\mathbf{u},\xi} - \hat{x}_{k|k-1})^2 + (c_{k,j}^{\mathbf{u},\eta} - \hat{y}_{k|k-1})^2} \right]^2 \\ &\quad + \tilde{\sigma}_{yy}^2 \left[\frac{c_{k,j}^{\mathbf{u},\xi} - \hat{x}_{k|k-1}}{(c_{k,j}^{\mathbf{u},\xi} - \hat{x}_{k|k-1})^2 + (c_{k,j}^{\mathbf{u},\eta} - \hat{y}_{k|k-1})^2} \right]^2 \\ &\quad + \tilde{\sigma}_{\phi\phi}^2 \end{aligned} \quad (27)$$

where $\tilde{\sigma}_{c1}^2, \tilde{\sigma}_{c2}^2, \tilde{\sigma}_{xx}^2, \tilde{\sigma}_{yy}^2$ and $\tilde{\sigma}_{\phi\phi}^2$ are given as

$$R_{k,j}^{\mathbf{u},\text{sim}} = \text{eig}[R_{k,j}^{\mathbf{u}}] = \begin{bmatrix} \tilde{\sigma}_{c1}^2 & 0 \\ 0 & \tilde{\sigma}_{c2}^2 \end{bmatrix} \quad (28)$$

$$P_{\mathcal{I}}^{\text{sim}} = \text{eig}[P_{\mathcal{I}}] = \begin{bmatrix} \tilde{\sigma}_{xx}^2 & 0 & 0 \\ 0 & \tilde{\sigma}_{yy}^2 & 0 \\ 0 & 0 & \tilde{\sigma}_{\phi\phi}^2 \end{bmatrix} \quad (29)$$

where $\text{eig}[\cdot]$ denotes the eigendecomposition operator. $R_{k,j}^{\mathbf{u}}$ is the converted measurement noise covariance via UCM technique, see “Appendix 1”. Also $P_{\mathcal{I}} \in \mathcal{R}^{3 \times 3}$ is the predicted state covariance matrix whose main diagonal elements are the variances of $\hat{x}_{k|k-1}$, $\hat{y}_{k|k-1}$ and $\hat{\phi}_{k|k-1}$, respectively.

4.2 Improved GP-PDA

In this subsection, an improved GP-PDA method is proposed for the problem of ETT in the clutter with polar measurements. Firstly, the predicted state and its covariance are obtained from the estimated state at the last time. Secondly, the original polar measurements are converted into linear measurements via the UCM technique. And three implementations are presented to approximate the prediction distribution of GP and hence to predict measurements accounting for the input uncertainty. Thirdly, the validation gate is constructed to select the validated measurement. Last, the probabilities of all feasible association events are calculated to update the state and its covariance. The algorithm flowchart is shown in Fig. 3.

Step 1: State prediction

Given the state estimate $\hat{\mathcal{X}}_{k-1}$ and the corresponding covariance P_{k-1} at time $k-1$, the predicted state $\hat{\mathcal{X}}_{k|k-1}$ and covariance $P_{k|k-1}$ can be calculated as

$$\hat{\mathcal{X}}_{k|k-1} = F_{k-1} \hat{\mathcal{X}}_{k-1} \quad (30)$$

$$P_{k|k-1} = F_{k-1} P_{k-1} F_{k-1}^\top + Q_{k-1} \quad (31)$$

Thus, one can obtain $\hat{x}_{k|k-1}$, $\hat{y}_{k|k-1}$ and $\hat{\phi}_{k|k-1}$ from $\hat{\mathcal{X}}_{k|k-1}$, and obtain $P_{\mathcal{I}}$ from $P_{k|k-1}$.

Step 2: Measurement prediction

Given the original polar measurement $c_{k,j}$ and its variance R^{pol} , $1 \leq j \leq M_k$, where M_k is the number of measurements at time k . They can be converted from polar to Cartesian coordinates via the UCM technique [37], see “Appendix 1”. Denote the converted measurement and its variance as $c_{k,j}^u$ and $R_{k,j}^u$, respectively.

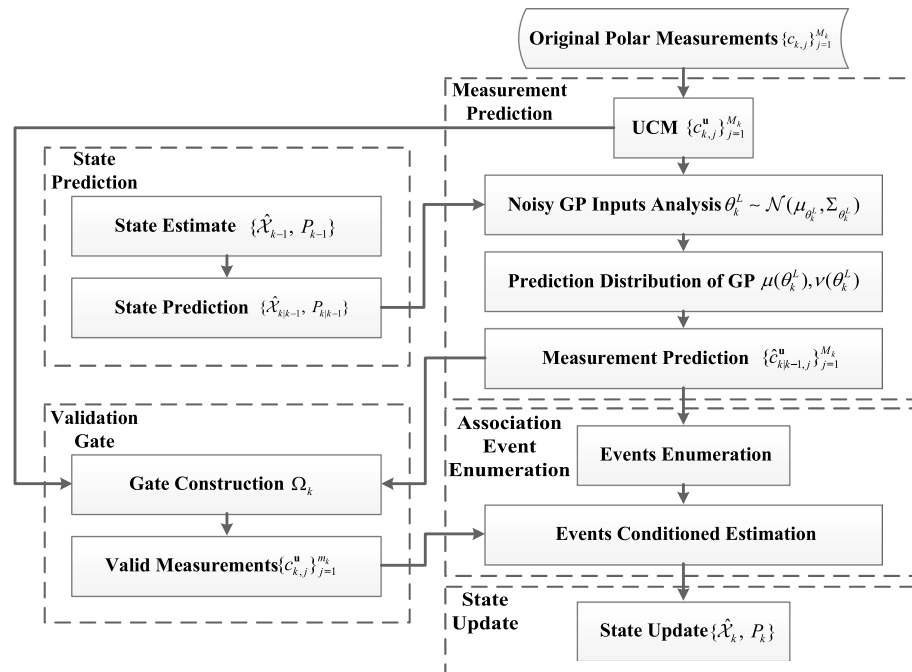


Fig. 3 Block diagram of the IGP-PDA

Using $c_{k,j}^u$, $R_{k,j}^u$, $\hat{x}_{k|k-1}$, $\hat{y}_{k|k-1}$, $\hat{\phi}_{k|k-1}$ and $P_{\mathcal{I}}$, the first two moments of the GP input $\hat{\theta}_{k,j}^L$, i.e., $\mu_{\theta_{k,j}^L}$ and $\Sigma_{\theta_{k,j}^L}$, can be estimated as described in Sect. 4.1. Thus, the predicted measurement $\hat{c}_{k|k-1,j}^u$ and the corresponding covariance of the measurement noise $\hat{R}_{k,j}^u$ are given as

$$\hat{c}_{k|k-1,j}^u = \hat{\mathbf{x}}_{k|k-1}^c + \hat{\mathbf{p}}_{k,j} \mu_{\text{IGP}}(\hat{\theta}_{k,j}^L) \quad (32)$$

$$\hat{R}_{k,j}^u = R_{k,j}^u + (\hat{\mathbf{p}}_{k,j}) \nu_{\text{IGP}}(\hat{\theta}_{k,j}^L) (\hat{\mathbf{p}}_{k,j})^\top \quad (33)$$

where $\hat{\mathbf{p}}_{k,j} = [\cos(\mu_{\theta_{k,j}^L} + \hat{\phi}_{k|k-1}), \sin(\mu_{\theta_{k,j}^L} + \hat{\phi}_{k|k-1})]^\top$ is the orientation vector, and $\hat{\mathbf{x}}_{k|k-1}^c = [\hat{x}_{k|k-1}, \hat{y}_{k|k-1}]^\top$ the predicted position of target centroid. Also $\mu_{\text{IGP}}(\hat{\theta}_{k,j}^L)$ and $\nu_{\text{IGP}}(\hat{\theta}_{k,j}^L)$ denote the mean and covariance of the GP predicted distribution with uncertain input, respectively. According to Sect. 2.2, the analytical solution to the predicted distribution is intractable [32]. In the following, three sub-optimal implementations are invoked to approximate $\mu_{\text{IGP}}(\hat{\theta}_{k,j}^L)$ and $\nu_{\text{IGP}}(\hat{\theta}_{k,j}^L)$.

(1) Sigma sampling (SS) method [38]:

$$\mu_{\text{IGP}}(\hat{\theta}_{k,j}^L) \approx \mu_{\text{SS}}(\hat{\theta}_{k,j}^L) = \sum_{i=0}^{2n} \omega_k^{m,(i)} \mu_{\text{SGP}}(\hat{\theta}_{k,j}^{L,(i)}) \quad (34)$$

$$\begin{aligned} \nu_{\text{IGP}}(\hat{\theta}_{k,j}^L) &\approx \nu_{\text{SS}}(\hat{\theta}_{k,j}^L) \\ &= \sum_{i=0}^{2n} \omega_k^{c,(i)} \left[\mu_{\text{SS}}(\hat{\theta}_{k,j}^L) - \mu_{\text{SGP}}(\hat{\theta}_{k,j}^{L,(i)}) \right] \left[\mu_{\text{SS}}(\hat{\theta}_{k,j}^L) - \mu_{\text{SGP}}(\hat{\theta}_{k,j}^{L,(i)}) \right]^\top \end{aligned} \quad (35)$$

where $\hat{\theta}_{k,j}^{L,(i)}$, $\omega_k^{m,(i)}$ and $\omega_k^{c,(i)}$ are the i th determined sampling point, its mean weight and covariance weight, respectively, n is the dimension of $\hat{\theta}_{k,j}^L$. More details see ‘‘Appendix 2’’. In addition, $\mu_{\text{SGP}}(\hat{\theta}_{k,j}^{L,(i)})$ is the mean of standard GP predicted distribution. According to (4), one has

$$\mu_{\text{SGP}}(\hat{\theta}_{k,j}^{L,(i)}) = K(\hat{\theta}_{k,j}^{L,(i)}, \Theta) [K(\Theta, \Theta)]^{-1} \hat{\mathbf{x}}_{k|k-1}^f \quad (36)$$

where $\hat{\mathbf{x}}_{k|k-1}^f$ is the predicted contour state obtained from $\hat{\mathcal{X}}_{k|k-1}$.

(2) Monte-Carlo (MC) method [41]:

$$\mu_{\text{IGP}}(\hat{\theta}_{k,j}^L) \approx \mu_{\text{MC}}(\hat{\theta}_{k,j}^L) = \frac{1}{N_{\text{MC}}} \sum_{i=1}^{N_{\text{MC}}} \mu_{\text{SGP}}(\hat{\theta}_{k,j}^{L,(i)}) \quad (37)$$

$$\begin{aligned} \nu_{\text{IGP}}(\hat{\theta}_{k,j}^L) &\approx \nu_{\text{MC}}(\hat{\theta}_{k,j}^L) \\ &= \frac{1}{N_{\text{MC}}} \sum_{i=1}^{N_{\text{MC}}} \left[\mu_{\text{MC}}(\hat{\theta}_{k,j}^L) - \mu_{\text{SGP}}(\hat{\theta}_{k,j}^{L,(i)}) \right] \left[\mu_{\text{MC}}(\hat{\theta}_{k,j}^L) - \mu_{\text{SGP}}(\hat{\theta}_{k,j}^{L,(i)}) \right]^\top \end{aligned} \quad (38)$$

where $\hat{\theta}_{k,j}^{L,(i)}$ is the i th random sampling point drawn from the Gaussian distribution $\mathcal{N}(\mu_{\theta_{k,j}^L}, \Sigma_{\theta_{k,j}^L})$ via the MC sampling technique, and N_{MC} is the number of sampling points. Similarly, $\mu_{SGP}(\hat{\theta}_{k,j}^{L,(i)})$ can be calculated by (36).

(3) Taylor Series (TS) method [34]:

According to (10) and (12), one has

$$\mu_{IGP}(\hat{\theta}_{k,j}^L) \approx \mu_{TS}(\hat{\theta}_{k,j}^L) = \mathbb{E}_{\hat{\theta}_{k,j}^L} [\mu_{SGP}(\hat{\theta}_{k,j}^L)] = \mu_{SGP}(\mu_{\theta_{k,j}^L}) \quad (39)$$

$$\begin{aligned} v_{IGP}(\hat{\theta}_{k,j}^L) &\approx v_{TS}(\hat{\theta}_{k,j}^L) = \mathbb{E}_{\hat{\theta}_{k,j}^L} [v_{SGP}(\hat{\theta}_{k,j}^L)] + \text{var}_{\hat{\theta}_{k,j}^L} [\mu_{SGP}(\hat{\theta}_{k,j}^L)] \\ &= v_{SGP}(\mu_{\theta_{k,j}^L}) + \frac{\partial \mu_{SGP}(\mu_{\theta_{k,j}^L})^\top}{\partial \mu_{\theta_{k,j}^L}} \Sigma_{\theta_{k,j}^L} \frac{\partial \mu_{SGP}(\mu_{\theta_{k,j}^L})}{\partial \mu_{\theta_{k,j}^L}} \end{aligned} \quad (40)$$

where $v_{SGP}(\mu_{\theta_{k,j}^L})$ is covariance of standard GP predicted distribution. According to (5), one has

$$v_{SGP}(\mu_{\theta_{k,j}^L}) = \kappa(\mu_{\theta_{k,j}^L}, \mu_{\theta_{k,j}^L}) - K(\mu_{\theta_{k,j}^L}, \Theta)[K(\Theta, \Theta)]^{-1}K(\Theta, \mu_{\theta_{k,j}^L}) \quad (41)$$

Substituting the above approximations of $\mu_{IGP}(\hat{\theta}_{k,j}^L)$ and $v_{IGP}(\hat{\theta}_{k,j}^L)$ into (32) and (33), one has the predicted measurement $\hat{c}_{k|k-1,j}^u$ and the corresponding covariance $\hat{R}_{k,j}^u$.

Step 3: Validation gate

Because an extended target has multiple scattering points and hence multiple measurements per scan, its validation gate can be constructed as a union of multiple validation sub-gates. Each sub-gate is centered on one of the predicted measurements $\hat{c}_{k|k-1,j}^u$. The j th converted measurement $c_{k,j}^u$ is considered as a validated measurement if it falls within the following sub-gate $\Omega_{k,j}$:

$$\Omega_{k,j} = \{c_{k,j}^u : [(c_{k,j}^u - \hat{c}_{k|k-1,j}^u)]^\top [S_{k,j}]^{-1} [(c_{k,j}^u - \hat{c}_{k|k-1,j}^u)] \leq g^2\} \quad (42)$$

In the above, g is the gate parameter and $S_{k,j}$ is the measurement innovation covariance,

$$S_{k,j} = H_{k,j} P_{k|k-1} (H_{k,j})^\top + \hat{R}_{k,j}^u \quad (43)$$

where $H_{k,j}$ is the Jacobian matrix of $\mathbf{h}_{k,j}^{\text{car}}(\cdot)$ evaluated at $\mathcal{X}_{k|k-1}$. Assume that there are m_k validated measurements at time k , the overall validation gate can be expressed as $\Omega_k = \bigcup_{j=1}^{m_k} \Omega_{k,j}$. More details see [26].

Step 4: Association event enumeration and state update

Given the m_k validated measurements, the total number of association events is 2^{m_k} . Let $A_{k,\psi}^{n_\psi}$ denote the n_ψ th association event where ψ out of m_k validated measurements are originated from targets. The corresponding posterior probability $\gamma_{k,\psi}^{n_\psi}$ can be calculated as:

$$\gamma_{k,\psi}^{n_\psi} = \frac{1}{c} p(c_k^u | A_{k,\psi}^{n_\psi}, m_k, \hat{\mathcal{X}}_{k|k-1}, \hat{P}_{k|k-1}) p(A_{k,\psi}^{n_\psi} | m_k) \quad (44)$$

where c is the normalization constant that is obtained by summing the numerators over all association events $A_{k,\psi}^{n_\psi}$. And the two terms in (44) are expressed as:

$$p(c_k^u | A_{k,\psi}^{n_\psi}, m_k, \hat{\mathcal{X}}_{k|k-1}, \hat{P}_{k|k-1}) = \begin{cases} (P_G)^{-1} (V_k)^{m_k+\psi} \mathcal{N}(0, S_{k,\psi}^{\psi, n_\psi}), \\ \psi = 1, \dots, m_k; n_\psi = 1, \dots, C_{m_k}^\psi \\ (V_k)^{-m_k}, \\ \psi = 0; n_\psi = 1 \end{cases} \quad (45)$$

$$p(A_{k,\psi}^{n_\psi} | m_k) = \begin{cases} \frac{C_{m_k}^\psi P_D P_G \mu_t(\psi) \mu_F(m_k - \psi)}{\sum_{\psi=0}^{m_k} P_D P_G \mu_t(\psi) \mu_F(m_k - \psi)}, \\ \psi = 1, \dots, m_k; n_\psi = 1, \dots, C_{m_k}^\psi \\ \frac{(1 - P_D P_G) \mu_F(m_k)}{\sum_{\psi=0}^{m_k} P_D P_G \mu_t(\psi) \mu_F(m_k - \psi) + (1 - P_D P_G) \mu_F(m_k)}, \\ \psi = 0; n_\psi = 1 \end{cases} \quad (46)$$

where V_k , P_G , P_D , $\mu_t(\cdot)$ and $\mu_F(\cdot)$ are the volume of $\Omega_{k,j}$, gate probability, detection probability, the probability mass function of the number of target-originated measurements and that of the number of clutter measurements, respectively. The output estimate is obtained by summing all conditional estimates as

$$\hat{\mathcal{X}}_k = \sum_{\psi=0}^{m_k} \sum_{n_\psi=1}^{C_{m_k}^\psi} \hat{\mathcal{X}}_{k,\psi}^{n_\psi} \gamma_{k,\psi}^{n_\psi} \quad (47)$$

where $C_{m_k}^\psi = m_k! / [(m_k - \psi)! \psi!]$. And its covariance P_k are given by

$$P_k = \sum_{\psi=0}^{m_k} \sum_{n_\psi=1}^{C_{m_k}^\psi} \gamma_{k,\psi}^{n_\psi} [P_{k,\psi}^{n_\psi} + \hat{\mathcal{X}}_{k,\psi}^{n_\psi} (\hat{\mathcal{X}}_{k,\psi}^{n_\psi})^\top] - \hat{\mathcal{X}}_k \hat{\mathcal{X}}_k^\top \quad (48)$$

where $\hat{\mathcal{X}}_{k,\psi}^{n_\psi}$ and $P_{k,\psi}^{n_\psi}$ denote the posterior conditional estimate and its covariance on the association event $A_{k,\psi}^{n_\psi}$, respectively.

5 Performance analysis

In [26], the PCRLB of ETT in the presence of measurement origin uncertainty is first derived using the GP model. However, the result is somewhat over-optimistic since the input uncertainty of GP is omitted. In this section, we derive a more conservative PCRLB which takes into account the input uncertainty. Note that all formulas are evaluated at the true state of the target, which is only available for simulation cases. Let $\hat{\mathcal{X}}_k$ be the unbiased estimate of \mathcal{X}_k conditioned on the converted measurement set $c_{1:k}^u$. The PCRLB on the covariance P_k is the inverse of the Fisher information matrix (FIM) J_k . That is

$$P_k = \mathbb{E}[(\hat{\mathcal{X}}_k - \mathcal{X}_k)(\hat{\mathcal{X}}_k - \mathcal{X}_k)^\top] \geq (J_k)^{-1} \quad (49)$$

The FIM can be evaluated recursively by

$$J_k = (F_k J_{k-1} F_k^\top + Q_k)^{-1} + J_{c,k} \quad (50)$$

with the initial value $J_0 = (P_0)^{-1}$. The term $J_{c,k}$ is measurement contribution to the PCRLB and is defined as

$$J_{c,k} = \mathbb{E}[-\Delta_{\mathcal{X}_k}^{\mathcal{X}_k} \ln p(c_k^u | \mathcal{X}_k)] \quad (51)$$

where $p(c_k^u | \mathcal{X}_k)$ is the likelihood function. Assume that the number of target-originated measurements is ψ , the form of $J_{c,k}$ is given by [26]:

$$J_{c,k} = \hat{q}_2 [H_{k,\psi}]^\top (\hat{R}_{k,\psi}^u)^{-1} [H_{k,\psi}] \quad (52)$$

$$H_{k,\psi} = [(H_{k,1}^{\text{car}})^\top, \dots, (H_{k,i}^{\text{car}})^\top, \dots, (H_{k,\psi}^{\text{car}})^\top] \quad (53)$$

$$\hat{R}_{k,\psi}^u = \text{diag}\{\hat{R}_{k,1}^u, \dots, \hat{R}_{k,i}^u, \dots, \hat{R}_{k,\psi}^u\} \quad (54)$$

where \hat{q}_2 is the information reduction factor obtained by off-line Monte Carlo. More details about \hat{q}_2 refer to [26, 40]. In addition, $H_{k,i}^{\text{car}}$ denotes the Jacobian matrix of $\mathbf{h}_{k,i}^{\text{car}}(\mathcal{X}_k)$ and $\hat{R}_{k,i}$ is the predicted covariance of measurement noise. According to (33), the variance of GP with uncertain inputs is larger than standard GP, which leads to a smaller $J_{c,k}$ and results in a more conservative PCRLB. In addition, the derivation of \hat{q}_2 accounting for the GP input uncertainty is beyond the scope of this work, and it will be discussed for further research.

6 Results and discussion

In the simulation, the performance of the proposed methods named IGP-PDA-SS, IGP-PDA-MC, and IGP-PDA-TS, is evaluated in two scenarios to track a moving ship in benign and clutter cases, respectively. In both cases, the target follows a maneuvering motion and is monitored by a high-resolution radar, which is located at the origin in the global coordinates. To verify the effectiveness of the proposed methods, they are compared with the standard GP-PDA and with the derived PCRLB. The root-mean-square error (RMSE), the Mahalanobis distance (MD), and the elapsed time are used as performance metrics. In addition, the effect of measurement noise on the GP input uncertainty and the tracking performance is analyzed. 100 Monte Carlo runs are used on a PC with an i5-8250U CPU running at 1.60 GHz, and all algorithms are implemented in MATLAB.

6.1 ETT in benign case

In the first case, the performance of the proposed methods is tested in a benign environment where no clutter exists. The surveillance duration is 100 s. The ship follows a nearly constant velocity (CV) motion model from $k = 1$ s to $k = 30$ s. Then, it makes a coordinated turn of 90° from $k = 31$ s to $k = 80$ s and returns to a nearly CV model from $k = 81$ s to the end. The initial kinematic state of target is $X_0 = X_0^{\text{tru}} + \bar{X}_0$ with the corresponding covariance $P_0 = \text{diag}\{1 \text{ m}^2, 0.1 \text{ m}^2/\text{s}^2, 1 \text{ m}^2, 0.1 \text{ m}^2/\text{s}^2, 0.1 \text{ rad}^2/\text{s}^2, 0.001 \text{ rad}^2/\text{s}^2\}$, where $\bar{X}_0 \sim \mathcal{N}(0, P_0)$ and $X_0^{\text{tru}} = [10 \text{ m}, \sqrt{2} \text{ m/s}, 10 \text{ m}, 0 \text{ m/s}, 0 \text{ rad}, 0 \text{ rad/s}]^\top$. The scan period is $T = 1$ s. The process transition matrix and process noise covariance of kinematic state is given by

$$F^s = \begin{bmatrix} 1 & T \\ 0 & 1 \end{bmatrix} \otimes I_3 \quad (55)$$

$$Q^s = \begin{bmatrix} \frac{T^3}{3} & \frac{T^2}{2} \\ \frac{T^2}{2} & T \end{bmatrix} \otimes \text{diag}\{\sigma_q^2, \sigma_q^2, \sigma_{q\phi}^2\} \quad (56)$$

where \otimes denotes the Kronecker product and I_3 is a three-dimensional identity matrix. The term $\sigma_q = 0.1 \text{ m} \cdot \text{s}^{-3/2}$ and $\sigma_{q\phi} = 0.001 \text{ rad} \cdot \text{s}^{-3/2}$ denotes the standard deviations of the position and the heading process noise, respectively. In the measurements model, the standard deviation of the measurements is $\sigma_d = 0.1 \text{ m}$ and $\sigma_\beta = 0.0001 \text{ rad}$. The detection probability is $P_D = 0.95$ and the gating probability is $P_G = 0.99$. The volume of the surveillance region is $V_c = 150 \times \pi (\text{m} \cdot \text{rad})$, and the number of the measurements scattering points follows a Poisson distribution with expected cardinality per unit volume $\lambda_t = 2 \times 10^{-1} \text{ m}^{-2}$.

The extended target contour is assumed to be stationary during the surveillance. The number of contour points is set to $N = 12$, and the contour transition matrix is given as $F^f = I_N$ and $Q_k^f = 0$, where I_N is an $N \times N$ identity matrix. In addition, the initial contour state $f_0(\theta_{1:N}) = 2 \text{ m}$. The hyper-parameters of the GP is set to $\sigma_r = 2, \sigma_f = 1.5$, and $l = \pi/8$. The number of random sampling points in IGP-PDA-MC is $N_{MC} = 100$, and the parameters in the IGP-PDA-SS are as follows: $n = 1, \zeta = 0, \varpi = 2$ and $\alpha = \sqrt{2}$ [39].

Figure 4 shows the true and estimates contour/trajectory at time $k = 1, 25, 50, 75, 100 \text{ s}$, respectively. It can be seen that all methods achieve satisfied estimate accuracy in the benign case. Figure 5 illustrates the RMSE and PCRLB curves of the contour estimate with four methods. The left sub-figure represents the local PCRLB curves from $k = 70 \text{ s}$ to $k = 100 \text{ s}$, and the right one shows the local RMSE curves between the same interval. It can be seen that the contour estimate RMSE of the proposed methods is smaller than that of GP-PDA, and the proposed PCRLB is more conservative and reasonable. Moreover, the average RMSE and PCRLB of the target centroid estimate, the average RMSE and PCRLB of the contour estimate, Mahalanobis distance (MD) [35], and the elapsed

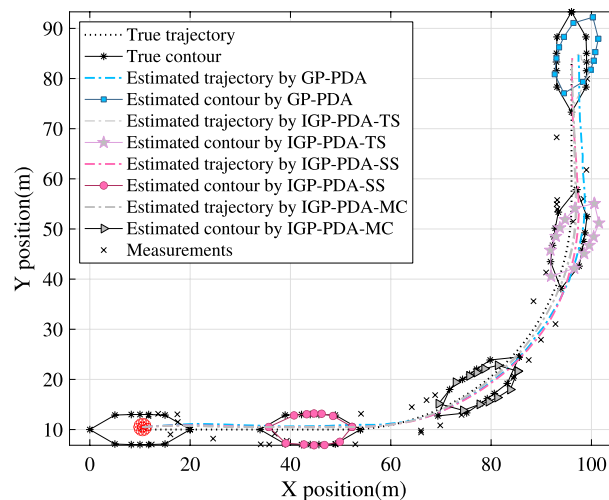


Fig. 4 True and estimates states in the first scenario

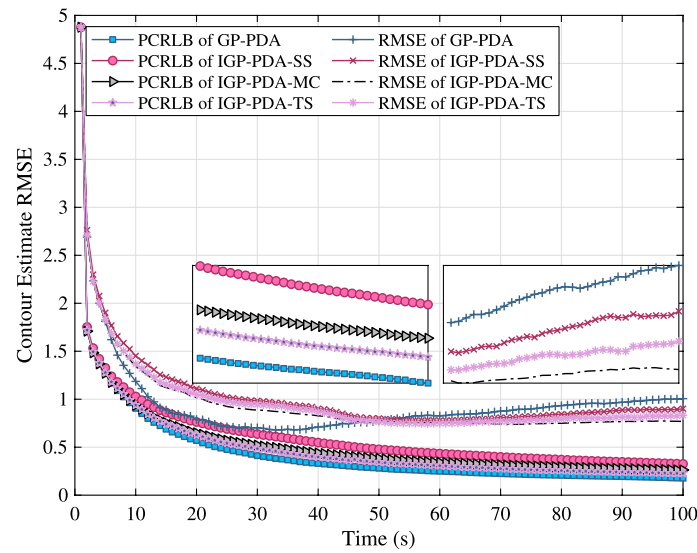


Fig. 5 Contour estimates: RMSE versus PCRLB in the first scenario

time per run of all methods are compared in Table 1. It shows that all proposed methods achieve better performance than GP-PDA in RMSE and MD. In addition, the proposed methods have a more conservative PCRLB by taking into account the GP input uncertainty. The elapsed time of the GP-PDA, IGP-PDA-SS, and IGP-PDA-TS is comparable and that of IGP-PDA-MC is longer. Figure 6 shows the error bars of the radius function estimates using different methods at $k = 100$ s. The solid red line represents the true value of the radius function and the error bar shows the twice standard deviations of the radius function distribution. It can be seen that the proposed methods have better posterior means than the standard GP-PDA. Also, the confidence intervals of the proposed methods can cover the true value better. In other words, the proposed methods achieve better estimate performance in the first-two moment than the standard GP-PDA by taking into account the input uncertainty. Among all methods, the IGP-PDA-MC provides the best coverage of the truth value.

Figure 7 shows the effect of measurement noise on input uncertainty. It can be seen that the input uncertainty Σ_{θ^L} is greatly affected by the measurement noise σ_d and σ_β . It increases as the measurement noise increases. Table 2 shows the average RMSE and PCRLB of the contour estimates against different σ_d and σ_β with four methods. It can be seen that as the measurement noise increases, the accuracy of the contour estimation decreases. For the same measurement noise level, the IGP-PDA-MC method achieves the smallest RMSE. Besides, the proposed methods have more conservative PCRLBs than GP-PDA. Similarly, Table 3 shows the centroid estimate RMSE and PCRLB. The result is consistent with the contour estimate, i.e., the proposed methods have smaller RMSE and more conservative PCRLB.

Table 4 compares the contour estimate MD and the elapsed time with different methods. It can be seen that the proposed methods take a significant performance advantage in MD. Among all the methods, the IGP-PDA-MC is the most time-consuming since lots of samples are required.

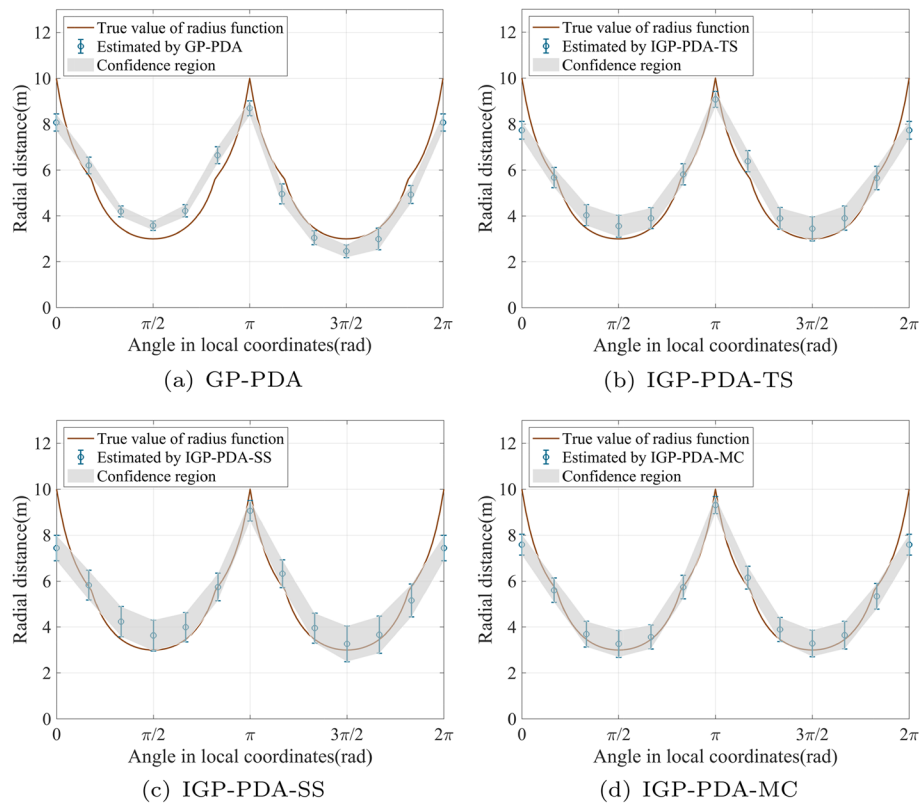


Fig. 6 True radius function and estimated error bar using different methods in the first scenario

Table 1 Performance of different models in the first scenario

	GP-PDA	IGP-PDA TS	IGP-PDA SS	IGP-PDA MC
Centroid estimate RMSE (m)	1.4221	1.2079	1.1543	1.0289
Centroid estimate PCRLB (m)	0.4141	0.5185	0.5560	0.5201
Contour estimate RMSE (m)	0.9203	0.8765	0.8404	0.8148
Contour estimate PCRLB (m)	0.1757	0.1879	0.2326	0.1986
MD	29.5479	23.2187	19.2746	20.2087
Elapsed time (s)	0.0346	0.0387	0.0396	2.9439

6.2 ETT in clutter case

In the second scenario, the methods are evaluated on a maneuvering ETT scenario in clutter. The number of clutter follows a Poisson distribution with expected cardinality per unit volume $\lambda_c = 2 \times 10^{-4}/(\text{m} \cdot \text{rad})$, and the other parameters as the same as those in the first scenario.

Figure 8 shows the true and estimates contour/trajectories at time $k = 1, 25, 50, 75, 100$ s, respectively. Figure 9 shows the RMSE and PCRLB curves of the average contour estimate with four methods. The left sub-figure represents the local PCRLB curves from $k = 70$ s to $k = 100$ s, and the right one shows the local

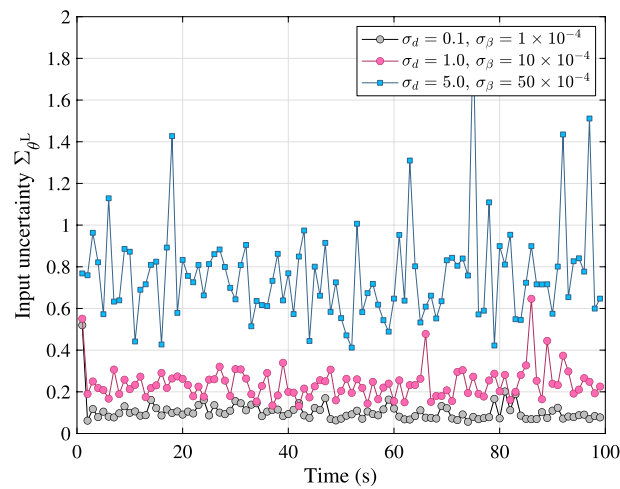


Fig. 7 Input uncertainty with different measurement noise

Table 2 Effect of measurement noise on contour estimates RMSE and PCRLB in first scenario

σ_d (m)	σ_β (rad)	RMSE (m)				PCRLB			
		GP-PDA	IGP-PDA TS	IGP-PDA SS	IGP-PDA MC	GP-PDA	IGP-PDA TS	IGP-PDA SS	IGP-PDA MC
1	0.001	1.2832	1.0297	1.0213	0.9359	0.4820	0.5990	0.7401	0.6426
5	0.005	2.8250	2.0623	1.9853	1.8798	0.9633	1.0433	0.9721	1.0686
10	0.010	4.1072	3.8698	3.4508	3.0291	1.1953	1.2886	1.1982	1.2361

Table 3 Effect of measurement noise on centroid estimates RMSE and PCRLB in first scenario

σ_d (m)	σ_β (rad)	RMSE (m)				PCRLB			
		GP-PDA	IGP-PDA TS	IGP-PDA SS	IGP-PDA MC	GP-PDA	IGP-PDA TS	IGP-PDA SS	IGP-PDA MC
1	0.001	2.9236	2.6238	2.5170	2.4002	0.6200	0.7437	0.7792	0.7110
5	0.005	5.5616	5.2095	5.1330	4.9046	0.8884	1.2280	1.1030	0.9139
10	0.010	7.1595	6.0202	5.7415	5.1747	1.3062	1.3993	1.4131	1.1853

Table 4 Effect of measurement noise on contour estimates MD and Elapsed time in first scenario

σ_d (m)	σ_β (rad)	MD				Elapsed time (s)			
		GP-PDA	IGP-PDA TS	IGP-PDA SS	IGP-PDA MC	GP-PDA	IGP-PDA TS	IGP-PDA SS	IGP-PDA MC
1	0.001	12.1956	8.2162	8.9578	7.4639	0.0619	0.0711	0.0745	0.4644
5	0.005	17.1469	8.7798	8.8804	8.2171	0.0617	0.0736	0.0720	0.5876
10	0.010	19.1075	9.8002	9.4223	9.3062	0.0713	0.0662	0.0769	0.4892

RMSE curves in the same interval. Figure 10 shows the error bars of the radius function estimated via different methods at $k = 100$ s. The conclusions are the same as those in the first scenario and are omitted here for brevity.

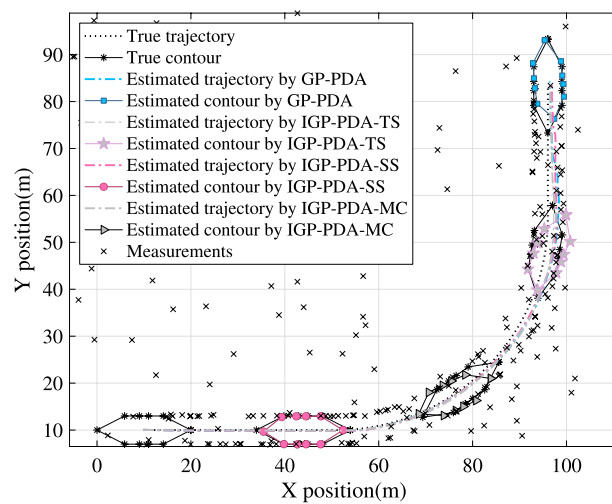


Fig. 8 True and estimates trajectories in the second scenario

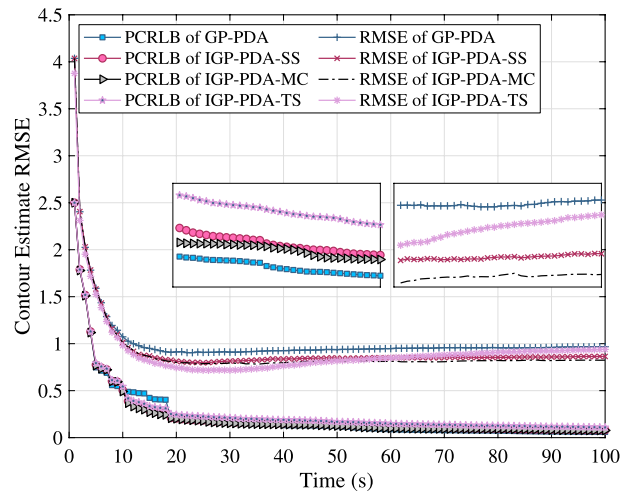


Fig. 9 Contour estimates: RMSE versus PCRLB in the second scenario

Tables 5 and 6 show the average RMSE and PCRLB of contour estimate and target centroid estimate via different methods against different measurement noise, respectively. Table 7 compares the contour estimate MD and the elapsed time with different methods against different measurement noise. We can obtain the same conclusions as those in the first scenario.

Tables 8 and 9 show the average RMSE and PCRLB of contour estimate and target centroid estimate against different clutter densities, respectively. Table 10 represents the MD and elapsed time. It can be seen that as the clutter density increases, the accuracy of the contour and centroid estimation decreases, and the computational load increases. For the same clutter level, the IGP-PDA-MC method achieves the best performance in RMSE and MD at the cost of more computation burden.

7 Conclusion and future work

In this paper, the IGP-PDA method is proposed to track an irregular-shape extended target in polar coordinates with measurement origin uncertainty. In the proposed method, the statistical property of input uncertainty is analyzed via the error propagation theory, and

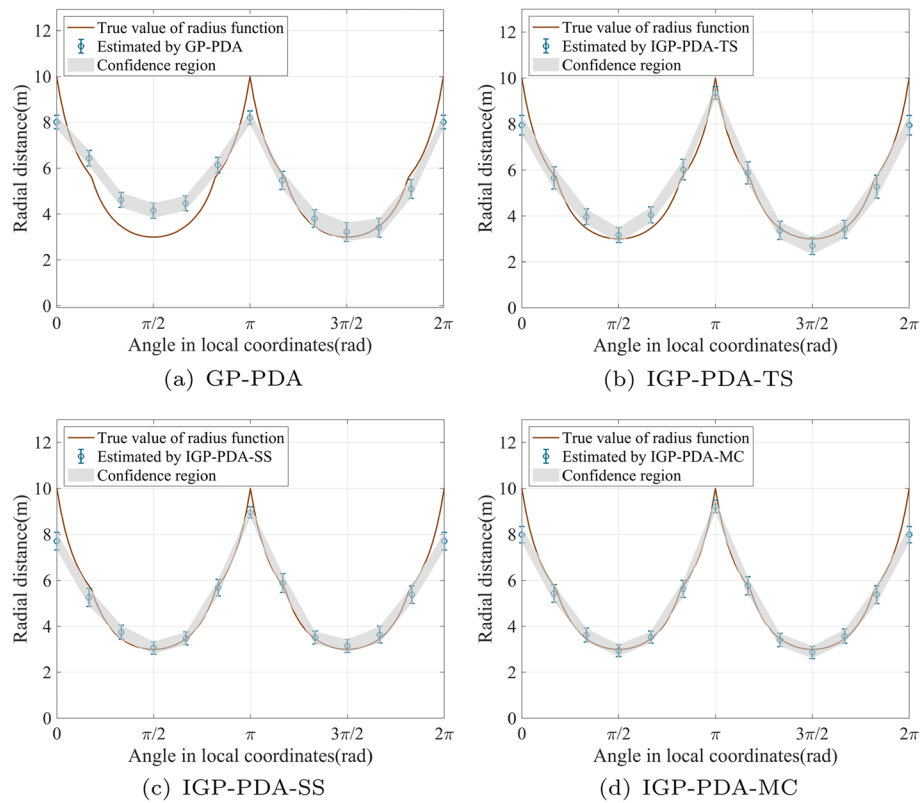


Fig. 10 True radius function and estimates error bar using different methods in the second scenario

Table 5 Effect of measurement noise on contour estimates RMSE and PCRLB in the second scenario

σ_d (m)	σ_β (rad)	RMSE (m)				PCRLB			
		GP-PDA	IGP-PDA TS	IGP-PDA SS	IGP-PDA MC	GP-PDA	IGP-PDA TS	IGP-PDA SS	IGP-PDA MC
1	0.001	1.9921	1.8859	1.5004	1.4916	0.2171	0.2989	0.2521	0.2734
5	0.005	3.1816	2.6085	2.5526	2.2322	0.3263	0.5866	0.4242	0.5446
10	0.010	4.9884	4.4195	4.1512	3.7823	0.5297	0.7559	0.5689	0.6382

Table 6 Effect of measurement noise on centroid estimates RMSE and PCRLB in the second scenario

σ_d (m)	σ_β (rad)	RMSE (m)				PCRLB			
		GP-PDA	IGP-PDA TS	IGP-PDA SS	IGP-PDA MC	GP-PDA	IGP-PDA TS	IGP-PDA SS	IGP-PDA MC
1	0.001	4.1884	3.9464	3.4769	3.1942	0.3573	0.4071	0.4751	0.4211
5	0.005	6.0819	5.8544	5.6209	5.1858	0.4275	0.5022	0.5011	0.4732
10	0.010	8.4704	8.3400	7.8537	7.2316	0.6415	0.7677	0.8094	0.7239

Table 7 Effect of measurement noise on contour estimates MD and elapsed time in the second scenario

σ_d (m)	σ_β (rad)	MD				Elapsed time (s)			
		GP-PDA	IGP-PDA TS	IGP-PDA SS	IGP-PDA MC	GP-PDA	IGP-PDA TS	IGP-PDA SS	IGP-PDA MC
1	0.001	12.4674	9.1948	8.3770	8.0933	0.4812	0.4302	0.4099	1.6175
5	0.005	12.6476	8.1813	9.0031	9.6871	0.5261	0.4863	0.3775	1.6928
10	0.010	17.1176	14.9349	15.2896	13.6653	0.5646	0.4917	0.5192	1.8638

Table 8 Effect of clutter density on contour estimates RMSE and PCRLB in the second scenario

λ_c (m · rad) ⁻¹	RMSE (m)				PCRLB (s)			
	GP-PDA	IGP-PDA TS	IGP-PDA SS	IGP-PDA MC	GP-PDA	IGP-PDA TS	IGP-PDA SS	IGP-PDA MC
4×10^{-4}	1.4481	1.3966	1.3109	1.3026	0.2896	0.3659	0.3464	0.3239
6×10^{-4}	1.5706	1.5633	1.4267	1.3773	0.2944	0.3931	0.3647	0.3298
8×10^{-4}	1.7354	1.6669	1.4919	1.3963	0.3078	0.4047	0.3973	0.3379

Table 9 Effect of clutter density on centroid estimates RMSE and PCRLB in the second scenario

λ_c (m · rad) ⁻¹	RMSE (m)				PCRLB (s)			
	GP-PDA	IGP-PDA TS	IGP-PDA SS	IGP-PDA MC	GP-PDA	IGP-PDA TS	IGP-PDA SS	IGP-PDA MC
4×10^{-4}	3.1906	2.8922	2.6846	2.0780	0.2486	0.3162	0.3031	0.2690
6×10^{-4}	3.7027	2.9171	3.0777	2.3545	0.2983	0.3454	0.3225	0.3029
8×10^{-4}	4.1441	3.1472	3.9250	3.1587	0.3596	0.3670	0.3375	0.3126

Table 10 Effect of clutter density on contour estimates MD and elapsed time in the second scenario

λ_c (m · rad) ⁻¹	MD				Elapsed time (s)			
	GP-PDA	IGP-PDA TS	IGP-PDA SS	IGP-PDA MC	GP-PDA	IGP-PDA TS	IGP-PDA SS	IGP-PDA MC
4×10^{-4}	19.5296	16.2759	15.9252	15.6275	0.4752	0.5931	0.4640	2.3628
6×10^{-4}	17.5733	10.5588	11.2339	10.0303	0.5723	0.6847	0.5062	3.2188
8×10^{-4}	16.7363	10.9033	13.7615	13.1029	0.5956	0.7535	0.4416	4.0414

then a more reasonable PCRLB of ETT is derived. Three approximation implementations are utilized to estimate the predicted distribution of GP with input uncertainty. Compared with the standard GP-PDA method, the IGP-PDA method achieves more accurate contour and kinematic estimates in the presence of clutter. The direction of future work includes analyzing the effect of input uncertainty on the IRF of PCRLB and reducing the number of feasible association events in heavy clutter.

Appendix 1

Unbiased converted measurement

Assume that $c_{k,j} = [d_{k,j}, \beta_{k,j}]$ is the polar measurements at time k with covariance $R^{\text{pol}} = \text{diag}\{\sigma_d^2, \sigma_\beta^2\}$. Using the unbiased converted measurement (UCM) technique [37], the converted measurements $c_{k,j}^{\text{u}}$ can be given as

$$c_{k,j}^{\text{u}} \triangleq \begin{bmatrix} c_{k,j}^{\text{u},\xi} \\ c_{k,j}^{\text{u},\eta} \end{bmatrix} = \lambda_\beta^{-1} \begin{bmatrix} d_{k,j} \cos \beta_{k,j} \\ d_{k,j} \sin \beta_{k,j} \end{bmatrix} \quad (1)$$

where $c_{k,j}^{\text{u},\xi}$ and $c_{k,j}^{\text{u},\eta}$ are the x -axis and y -axis position of measurements in Cartesian coordinates, respectively. And the term $\lambda_\beta = \exp(-\sigma_\beta^2/2)$ is the bias compensation factor [37]. The converted covariance $R_{k,j}^{\text{u}}$ is given by

$$R_{k,j}^{\text{u}} = \begin{bmatrix} R_{k,j}^{\text{u},11} & R_{k,j}^{\text{u},12} \\ R_{k,j}^{\text{u},21} & R_{k,j}^{\text{u},22} \end{bmatrix} \quad (2)$$

where

$$R_{k,j}^{\text{u},11} = \frac{1}{2}(d_{k,j}^2 + \sigma_d^2) [1 + \exp(-2\sigma_\beta^2) \cos(2\beta_{k,j})] + [\exp(\sigma_\beta^2) - 2] d_{k,j}^2 \cos^2(\beta_{k,j}) \quad (3)$$

$$R_{k,j}^{\text{u},22} = \frac{1}{2}(d_{k,j}^2 + \sigma_d^2) [1 - \exp(-2\sigma_\beta^2) \cos(2\beta_{k,j})] + [\exp(\sigma_\beta^2) - 2] d_{k,j}^2 \sin^2(\beta_{k,j}) \quad (4)$$

$$R_{k,j}^{\text{u},12} = R_{k,j}^{\text{u},21} = \frac{1}{2}(d_{k,j}^2 + \sigma_d^2) [\exp(-2\sigma_\beta^2) \sin(2\beta_{k,j})] + [\exp(\sigma_\beta^2) - 2] d_{k,j}^2 \cos(\beta_{k,j}) \sin(\beta_{k,j}) \quad (5)$$

Appendix 2

Sigma sampling

Assume that the GP input is a n -dimensional variable with distribution $\hat{\theta}_{k,j}^L \sim \mathcal{N}(\mu_{\theta_{k,j}}^L, \Sigma_{\theta_{k,j}}^L)$ (dimension n). The Sigma sampling points $\hat{\theta}_{k,j}^{L,(i)}$ are given as [38]

$$\hat{\theta}_{k,j}^{L,(0)} = \mu_{\theta_{k,j}}^L \quad (6)$$

$$\hat{\theta}_{k,j}^{L,(i)} = \mu_{\theta_{k,j}}^L + \left(\sqrt{(n+\lambda)\Sigma_{\theta_{k,j}}^L} \right)_i \quad i = 1, \dots, n \quad (7)$$

$$\hat{\theta}_{k,j}^{L,(i)} = \mu_{\theta_{k,j}}^L - \left(\sqrt{(n+\lambda)\Sigma_{\theta_{k,j}}^L} \right)_i \quad i = n+1, \dots, 2n \quad (8)$$

The mean weights $\omega_k^{m,(i)}$ and the covariance weights $\omega_k^{c,(0)}$ are given as

$$\omega_k^{m,(0)} = \lambda/(n + \lambda) \quad (9)$$

$$\omega_k^{c,(0)} = \lambda/(n + \lambda) + (1 - \alpha^2 + \varpi) \quad (10)$$

$$\omega_k^{m,(i)} = \omega_k^{c,(i)} = 1/[2(n + \lambda)] \quad i = 1, \dots, 2n \quad (11)$$

where $\lambda = \alpha^2(n + \varsigma) - n$ is a scaling parameter, α denotes the spread of the sigma points around the input mean value, ς is a secondary scaling parameter, and $\varpi = 2$ is optimal for Gaussian distribution [38].

Abbreviations

GP	Gaussian Processes
ETT	Extended Target Tracking
GP-ETT	GP-based ETT
GP-EKF	GP-based Extended Kalman Filter
GP-PDA	GP-based Probabilistic Data Association
IGP-PDA	Improved GP-based Probabilistic Data Association
SMC	Sequential Monte Carlo
RM	Random Matrix
RHM	Random Hypersurface Models
PCRLB	Posterior Cramer-Rao Lower Bound
UCM	Unbiased Converted Measurement
SS	Sigma Sampling
IGP-PDA-SS	Improved GP-PDA using Sigma Sampling method
MC	Monte-Carlo Sampling
IGP-PDA-MC	Improved GP-PDA using Monte-Carlo Sampling method
TS	Taylor Series method
IGP-PDA-TS	Improved GP-PDA using Taylor Series method
FIM	Fisher Information Matrix
RMSE	Root Mean Square Error
MD	Mahalanobis Distance
CV	Constant Velocity
IRF	Information Reduction Factor
$f(\cdot)$	Latent function
\mathbf{u}	Input set of GP
\mathbf{u}_*	Test input of GP
\mathbf{y}	Output set of GP
$\mathbf{a}(\cdot)$	Mean function of GP
$\kappa(\cdot, \cdot)$	Covariance function of GP
$\mathbf{K}(\cdot, \cdot)$	Covariance matrix of GP
$\mu_{\text{SGP}}(\cdot)$	Predictive mean of standard GP
$\nu_{\text{SGP}}(\cdot)$	Predictive covariance of standard GP
$\mu_{\mathbf{u}_*}$	Mean of GP input
$\Sigma_{\mathbf{u}_*}$	Covariance of GP input
$\mu_{\text{IGP}}(\cdot)$	Predictive mean of GP with uncertain input
$\nu_{\text{IGP}}(\cdot)$	Predictive covariance of GP with uncertain input
\mathcal{X}	Extended target state
Θ	Angle of contour points
z	Position of scattering point
c	Original measurement
χ	Clutter
$c^{\mathbf{u}}$	Converted measurement via UCM
$\mathbf{h}^{\text{pol}}(\cdot)$	Nonlinear measurement function in polar coordinates
$\mathbf{h}^{\text{car}}(\cdot)$	Measurement function in Cartesian coordinates
\mathbf{R}^{pol}	Covariance of the original measurement
$\mathbf{R}^{\mathbf{u}}$	Covariance of the converted measurement
$\hat{\mathbf{R}}^{\mathbf{u}}$	Covariance of the predicted measurement

Acknowledgements

Not applicable.

Author information's

Yunfei Guo received the B.S. degree in electrical engineering from Yanshan University, China, in 2002, and the Ph.D. degree in electrical engineering from Zhejiang University, China, in 2007. From 2014 to 2015, he was a Visiting Professor with McMaster University, Canada. He is currently a Professor with the School of Automation, Hangzhou Dianzi University, Hangzhou. He is also serving as the Deputy Secretary General with the China Information Fusion Society. His research interests include target tracking, information fusion, and Gaussian processes.

Dongsheng Yang received the B.S. and M.S. degrees in automation from Anhui Polytechnic University, Wuhu, China, and Shenyang university of chemical technique, Shenyang, China, in 2018 and 2021, respectively, and he is currently working toward the Ph.D. degree with the School of Automation in Hangzhou Dianzi University. His research interests include extended target tracking and information fusion.

Lei Ren received the B.S. degree in automation in 2019 from Hangzhou Dianzi University, Hangzhou, China, and he is currently working toward the Postgraduate degree with the School of Automation. His research interests include extended target tracking.

Lei Yan received the B.S. degree in automation in 2020 from Hangzhou Dianzi University, Hangzhou, China, and he is currently working toward the Postgraduate degree with the School of Automation. His research interests include target tracking.

Author contributions

YG was in charge of the whole trial; DY wrote the manuscript; LR and LY assisted with sampling and laboratory analyses. All authors read and approved the final manuscript.

Funding

Supported by Zhejiang Provincial Natural Science Foundation of China (Grant No. LZ20F010002), and by Zhejiang Provincial Science and Technology Project (Grant No. 2022C01095).

Availability of data and materials

Not applicable.

Declarations**Ethics approval and consent to participate**

Not applicable.

Consent for publication

Not applicable.

Competing interests

The authors declare that they have no competing interests.

Received: 22 May 2022 Accepted: 18 October 2022

Published online: 29 October 2022

References

1. Y. Liu, H. Ji, Y. Zhang, Measurement transformation algorithm for extended target tracking. *Signal Process.* **186**, 108129 (2021). <https://doi.org/10.1016/j.sigpro.2021.108129>
2. K. Thormann, M. Baum, J. Honer, Extended target tracking using Gaussian processes with high-resolution automotive radar, in *21st International Conference on Information Fusion* (2018), pp. 1764–1770. <https://doi.org/10.23919/ICIF.2018.8455630>
3. Z. Qin, T. Kirubarajan, Y. Liang, Application of an efficient graph-based partitioning algorithm for extended target tracking using GM-PHD filter. *IEEE Trans. Aerosp. Electron. Syst.* **56**, 4451–4466 (2020). <https://doi.org/10.1109/TAES.2020.2990803>
4. M. Michaelis, P. Berthold, D. Meissner, H.-J. Wuensche, Heterogeneous multi-sensor fusion for extended objects in automotive scenarios using Gaussian processes and a GMPHD-filter. *Sens. Data Fusion Trends Solut. Appl.* **2017**, 1–6 (2017). <https://doi.org/10.1109/SDF.2017.8126351>
5. F. Li, I. Shugurov, B. Busam, M. Li, S. Yang, S. Ilic, PolarMesh: a star-convex 3D shape approximation for object pose estimation. *IEEE Robot. Autom. Lett.* **7**, 4416–4423 (2022). <https://doi.org/10.1109/LRA.2022.3147880>
6. Y. Guo, Y. Li, A. Xue, R. Tharmarasa, T. Kirubarajan, Simultaneous tracking of a maneuvering ship and its wake using Gaussian processes. *Signal Process.* **172**, 107547 (2020). <https://doi.org/10.1016/j.sigpro.2020.107547>
7. S. Yang, M. Baum, Tracking the orientation and axes lengths of an elliptical extended object. *IEEE Trans. Signal Process.* **67**, 4720–4729 (2019). <https://doi.org/10.1109/TSP.2019.2929462>
8. X. Jiang, F.R. Yu, T. Song, Z. Ma, Y. Song, D. Zhu, Blockchain-enabled cross-domain object detection for autonomous driving: a model sharing approach. *IEEE Internet Things J.* **7**, 3681–3692 (2020)
9. M. Kumru, E. Ozkan, 3D extended object tracking using recursive Gaussian processes, in *21st International Conference on Information Fusion* (2018), pp. 1–8. <https://doi.org/10.23919/ICIF.2018.8455480>

10. M. Kumru, E. Ozkan, Three-dimensional extended object tracking and shape learning using Gaussian processes. *IEEE Trans. Aerosp. Electron. Syst.* **57**, 2795–2814 (2021). <https://doi.org/10.1109/TAES.2021.3067668>
11. K. Granström, M. Baum, S. Reuter, Extended object tracking: introduction, overview, and applications. *J. Adv. Inf. Fusion* **12**, 139–174 (2017)
12. J. Vermaak, N. Ikoma, S. Godsill, Sequential Monte Carlo framework for extended object tracking. *IEEE Proc. Radar Sonar Navig.* **152**, 353–363 (2005). <https://doi.org/10.1049/ip-rsn:20045044>
13. L. Mihaylova, A.Y. Carmi, F. Septier, A. Gning, S.K. Pang, S. Godsill, Overview of Bayesian sequential Monte Carlo methods for group and extended object tracking. *Digital Signal Process.* **25**, 1–16 (2014)
14. J.W. Koch, Bayesian approach to extended object and cluster tracking using random matrices. *IEEE Trans. Aerosp. Electron. Syst.* **44**, 1042–1059 (2008). <https://doi.org/10.1109/TAES.2008.4655362>
15. J. Lan, X.R. Li, Tracking of maneuvering non-ellipsoidal extended object or target group using random matrix. *IEEE Trans. Signal Process.* **62**, 2450–2463 (2014). <https://doi.org/10.1109/TSP.2014.2309561>
16. J. Lan, X.R. Li, Tracking of extended object or target group using random matrix: new model and approach. *IEEE Trans. Aerosp. Electron. Syst.* **52**, 2973–2989 (2016). <https://doi.org/10.1109/TAES.2016.130346>
17. N.J. Bartlett, C. Renton, A.G. Wills, A closed-form prediction update for extended target tracking using random matrices. *IEEE Trans. Signal Process.* **68**, 2404–2418 (2020). <https://doi.org/10.1109/TSP.2020.2984390>
18. P. Hoher, S. Wirtensohn, T. Baur, J. Reuter, F. Govaers, W. Koch, Extended target tracking with a lidar sensor using random matrices and a virtual measurement model. *IEEE Trans. Signal Process.* **70**, 228–239 (2022)
19. M. Baum, B. Noack, U.D. Hanebeck, Extended object and group tracking with elliptic random hypersurface models, in *13th International Conference on Information Fusion* (2010), pp. 1–8. <https://doi.org/10.1109/ICIF.2010.5711854>
20. M. Baum, U.D. Hanebeck, Extended object tracking with random hypersurface models. *IEEE Trans. Aerosp. Electron. Syst.* **50**, 149–159 (2014). <https://doi.org/10.1109/TAES.2013.120107>
21. X. Zhang, Z. Yan, Y. Chen, Y. Yuan, A novel particle filter for extended target tracking with random hypersurface model. *Appl. Math. Comput.* **425**, 127081 (2022). <https://doi.org/10.1016/j.amc.2022.127081>
22. N. Wahlström, E. ozkan, Extended target tracking using Gaussian processes. *IEEE Trans. Signal Process.* **63**, 4165–4178 (2015). <https://doi.org/10.1109/TSP.2015.2424194>
23. W. Aftab, R. Hostettler, A. De Freitas, M. Arvaneh, L. Mihaylova, Spatio-temporal Gaussian process models for extended and group object tracking with irregular shapes. *IEEE Trans. Veh. Technol.* **68**, 2137–2151 (2019). <https://doi.org/10.1109/TVT.2019.2891006>
24. C.K. Williams, C.E. Rasmussen, *Gaussian Processes for Machine Learning*, vol. 2 (MIT Press, Cambridge, 2006)
25. T. Hirscher, A. Scheel, S. Reuter, K. Dietmayer, Multiple extended object tracking using gaussian processes, in *19th International Conference on Information Fusion (FUSION)* (2016), pp. 868–875
26. Y. Guo, Y. Li, R. Tharmarasa, T. Kirubarajan, M. Efe, B. Sarikaya, GP-PDA filter for extended target tracking with measurement origin uncertainty. *IEEE Trans. Aerosp. Electron. Syst.* **55**, 1725–1742 (2019). <https://doi.org/10.1109/TAES.2018.2875555>
27. J.E. Johnson, V. Laparra, G. Camps-Valls, Accounting for input noise in Gaussian process parameter retrieval. *IEEE Geosci. Remote Sens. Lett.* **17**, 391–395 (2020). <https://doi.org/10.1109/LGRS.2019.2921476>
28. K. Kersting, C. Plagemann, P. Pfaff, W. Burgard, Most-likely heteroscedastic Gaussian process regression. **227**, 393–400 (2007). <https://doi.org/10.1145/1273496.1273546>
29. M. Lazaro-Gredilla, M. Titsias, Variational heteroscedastic Gaussian process regression, in *Proceedings of the 28th International Conference on Machine Learning* (2011), pp. 841–848. <https://doi.org/10.5555/3104482.3104588>
30. L. Munoz-Gonzalez, M. Lazaro-Gredilla, A.R. Figueiras-Vidal, Laplace approximation for divisive Gaussian processes for nonstationary regression. *IEEE Trans. Pattern Anal. Mach. Intell.* **38**, 618–624 (2016). <https://doi.org/10.1109/TPAMI.2015.2452914>
31. A. Girard, C. Rasmussen, R. Murray-Smith, *Gaussian Process Priors with Uncertain Inputs: Multiple-Step-Ahead Prediction* (School of Computing Science, 2002)
32. A. Girard, C. E. Rasmussen, J. Q. Candela, R. Murray-Smith, Gaussian process priors with uncertain inputs application to multiple-step ahead time series forecasting, in *Proceedings of the 15th International Conference on Neural Information Processing Systems* (2002), pp. 545–552. <https://doi.org/10.5555/2968618.2968686>
33. J.Q. Candela, A. Girard, C. Rasmussen, Prediction at an uncertain input for Gaussian processes and relevance vector machines application to multiple-step ahead time-series forecasting. Technical University of Denmark (2003)
34. A. Girard, R. Murray-Smith, *Learning a Gaussian Process Model with Uncertain Inputs* (Department of Computing Science, University of Glasgow, Glasgow, 2003)
35. M.P. Deisenroth, M.F. Huber, U.D. Hanebeck, Analytic moment-based Gaussian process filtering, in *Proceedings of the 26th Annual International Conference on Machine Learning* (2009), pp. 225–232. <https://doi.org/10.1145/1553374.1553403>
36. A. Mchutchon, C. Rasmussen, Gaussian process training with input noise. *Adv. Neural. Inf. Process. Syst.* **24**, 1341–1349 (2011). <https://doi.org/10.5555/2986459.2986609>
37. M. Longbin, S. Xiaoquan, Z. Yiyu, S.Z. Kang, Y. Bar-Shalom, Unbiased converted measurements for tracking. *IEEE Trans. Aerosp. Electron. Syst.* **34**, 1023–1027 (1998). <https://doi.org/10.1109/7.705921>
38. S.J. Julier, J.K. Uhlmann, New extension of the Kalman filter to nonlinear systems. *Signal Process. Sens. Fusion Target Recogn. VI* **3068**, 182–193 (1997). <https://doi.org/10.1117/12.280797>
39. E. Wan, R. Van Der Merwe, The unscented Kalman filter for nonlinear estimation, in *Proceedings of the IEEE 2000 Adaptive Systems for Signal Processing, Communications, and Control Symposium* (2000), pp. 153–158. <https://doi.org/10.1109/ASSPCC.2000.882463>
40. C. Jauffret, Y. Bar-Shalom, Track formation with bearing and frequency measurements in clutter. *IEEE Trans. Aerosp. Electron. Syst.* **26**, 999–1010 (1990). <https://doi.org/10.1109/7.62252>
41. M. David, *Introduction to Monte Carlo Methods. Learning in Graphical Models* (1998), pp. 175–204

Publisher's Note

Springer Nature remains neutral with regard to jurisdictional claims in published maps and institutional affiliations.